Journal of Optics

Crossmark

RECEIVED
dd Month
yyyy

REVISED
dd Month
yyyy

PAPER

Low-Cost Dual Fabry-Pérot Cavities for High-Purity, Angle-Invariant Structural Color

Anya Li[1], Abdullah A. Mahmood[2], Jungtaek Kim[3], Guangyong Li[2], and Paul W. Leu[3,*]

[1]Early College at Guilford, Guilford College, Greensboro, USA
[2] Department of Electrical and Computer Engineering, University of Pittsburgh, Pittsburgh, USA.
[3] Department of Industrial Engineering, University of Pittsburgh, Pittsburgh, USA.

E-mail: pleu@pitt.edu

Keywords: Structural Colors, Reflectivity, Fabry-Pérot Cavities, Color Gamut, Inverse Design, Machine Learning

Abstract

Producing high-purity, angle-invariant structural colors with low-cost multilayer materials remains challenging. Here, we first examine analyze multilayer structures containing a single embedded Fabry-Pérot cavity and compare their reflective spectra. While these structures enhance optical absorption and supress parasitic reflections to generate a highly saturated blue, they are unable to produce pure green and red hues. To overcome these limitations, we propose and simulate several multilayer designs that incorporate dual Fabry-Pérot cavities, which can produce pure, saturated colors with high reflection efficiency. Using an inverse design approach, we identify optimal dual Fabry-Pérot structures comprised solely of low-cost materials that achieve high-purity colors fully spanning the sRGB color space (100%) with an additional 66% coverage, corresponding to 56% of the entire CIE 1931 color space. Our analysis confirms that dual Fabry-Pérot cavities play a critical role in producing this exceptional color purity, and the upper metal layers must have a good absorption in the blue and green region to obtain a pure red. Taking advantage of the high refractive index of the dielectric material, the identified structure also exhibits a vibrant angle-independent appearance with incident angles up to $\pm 45°$. This work presents a practical path toward manufacturing high-performance structural colors using low-cost materials, paving the way for their broad application in various fields, including display electronics, decoration, and anti-counterfeiting.

1 Introduction

The ability to generate and control color underpins an extraordinary range of technologies, including visual displays, imaging systems, optical communications, sensing, camouflage, and aesthetic coatings. Traditionally, color is produced by pigments and dyes that derive their appearance from wavelength-selective absorption governed by molecular composition. However, because their absorption bands are typically broad, pigments and dyes exhibit limited color purity and a restricted achievable color gamut. They also tend to degrade over time when exposed to ultraviolet light, heat, or harsh chemicals, and many organic dyes present toxicity and environmental hazards.

In contrast, structural colors arise from the physical interaction of light with subwavelength structures such as multilayers or metasurfaces [1, 2]. Since no chromophores are involved, structural colors exhibit excellent chemical stability and significant environmental benefits. Structural coloration is widely observed in nature [3], producing brilliant hues of insects, birds, marine organisms, and even certain mammals such as the mandrill. Due to their durability, environmental sustainability, and the ability to generate a wide and tunable color gamut, structural colors hold great promise for many applications [4], including display technologies [5, 6], inkless printing [7, 8], nanoimprinting [9, 10], decorative coatings [11], and anti-counterfeiting systems [12].

Metasurfaces can produce a remarkably wide range of highly saturated structural colors [5], with some demonstrations exceeding the full sRGB color space [13]. However, achieving such wide gamuts often requires expensive substrates, such as sapphire [13]. Moreover, the fabrication of metasurfaces typically relies on costly, non-scalable nanofabrication techniques such as electron-beam lithography. These processes are time-consuming and generally limited to small-area fabrication.

Multilayered structures offer a simple and cost-effective means for producing structural colors. In transmission, narrowband spectral responses that provide pure color can be realized using asymmetric Fabry–Pérot (FP) cavities, such as metal–insulator–metal (MIM) or metal–insulator–semiconductor (MIS) configurations [14, 15, 16, 17, 18]. Although FP cavities yield narrowband transmission that is well suited for high color–purity filters, they are less effective for reflective structural color because most of the spectrum is reflected, except for the narrow transmitted band. To improve reflection purity, the broadband background must be suppressed, which is often done by using lossy metals such as Cr [19, 15], Ni [20], Cu [17], Au [21, 22]; adding a lossy semiconductor layer such as Ge to enable Fano resonance [23]; or embedding a semiconductor absorber like $Ge_2Sb_2Te_5$ [24] or $Sc_{0.2}Sb_2Te_3$ [25] within the dielectric layer. Despite these efforts, achieving high-purity green and red remains difficult because higher-order resonances at shorter wavelengths enhance reflection in the blue-green region [26].

Adding an anti-reflection coating has proven effective in suppressing blue reflection [27, 28] and expanding the color gamut, especially in the green region. However, producing a pure red using multilayer thin films remains challenging. Saturated red reflective colors are not only difficult to obtain experimentally but are also absent in nature [29, 26]. Some beetles, such as *Torynorrhina flammea*, exhibit structural red hues, but these are less saturated and appear more burgundy than pure red. Recent efforts to achieve pure red using multilayer structures have explored several strategies, such as the use of exotic dielectrics such as WO_3 [30], embedding absorbers like Ge [31] or a-Si [32, 33], and employing 1D photonic crystals composed of alternating layers of a-Si or Ge with Si_3N_4 [34, 35]. These approaches are effective, with some of them achieving a red very close to the sRGB standard [30], but none have yet completely exceeded the sRGB color gamut. In addition, these solutions rely on exotic dielectric or semiconductor materials that require high-temperature deposition. Moreover, the optical constants of these specific materials are much more sensitive to microstructure and crystallinity than those of common metals or dielectric insulators.

Dual FP cavities have shown good potential to expand the color gamut using relatively easily accessible fabrication methods [36, 37]. However, current demonstrations face key limitations. In Kim *et al.*'s work [36], the authors successfully reproduce primary colors close to the primary red, green, and blue of the sRGB standard, but their colors do not exceed the sRGB gamut, and their dual-resonance stacks rely on Au, Ti, and Ag, which are comparatively expensive. Ghobadi *et al.*'s work [37] similarly does not achieve full sRGB coverage and requires a Ge semiconductor layer, introducing material cost and fabrication complexity. To date, dual-FP-cavity implementations have relied on costly metals or complex semiconductor materials. Most importantly, they have not produced gamuts that exceed sRGB in reflection.

To gain a deeper understanding of the effect of FP cavities on the purity of reflective structural colors, we compare the reflective spectra of a few multilayer structures with an MIM FP cavity using our recently developed inverse design approach [38]. This comparison confirms the critical role of the FP cavity in enhancing optical absorption and suppressing unwanted reflections. While MIM cavities can generate highly saturated blues, they are unable to produce highly saturated greens or reds due to parastic reflection at lower wavelengths. Based on this insight, we design a set of dual FP multilayer structures using a metal-insulator-metal-insulator-metal (MIMIM) architecture, made entirely of low-cost, readily available materials, and compatible with scalable fabrication techniques. These proposed structures are engineered to suppress unwanted reflections at targeted wavelengths while preserving the desired reflection peak, thereby expanding the reflective color gamut.

Our simulations validate the effectiveness of these designs with dual FP cavities. We identified two multilayer structures based on double FP structures comprised solely of TiO_2, Cu, and Ni with either an Fe or Cu substrate that successfully achieve saturated red, green, and blue primaries that extend beyond the sRGB standard with peak reflection efficiency close to or exceeding 70%. The optimized structures consist of TiO_2/Cu/TiO_2/Ni/TiO_2, deposited on either an Fe or Cu substrate. These structures provide full coverage of the sRGB space (100%) and expand the overall sRGB area by more than 62% and 66%, respectively. The color gamut coverage ranges of these two structures reach 52% and 56% of the entire CIE color space, respectively. A layer-by-layer absorption analysis confirms that the metal layers within the FP cavities suppress unwanted spectral components, resulting in the observed high color purity. We additionally evaluate the angular performance of the structure that achieves the largest color gamut. The resulting colors remain vivid and nearly angle-invariant for incident angles up to $\pm 45°$, as quantified by CIEDE2000 based on the CIELAB color space. This favorable angular stability arises from the high refractive index of the TiO_2 dielectric layers, which helps to maintain a consistent optical path difference across a wide range of viewing angles.

2 Methods

The color gamut of the subwavelength multilayered structures in this study is determined through forward simulation and inverse design, which we have previously developed and are detailed in the following.

2.1 Forward Simulations

We use our JaxLayerLumos software package [39] to perform forward simulations of light interacting with subwavelength multilayer structures. The package implements the transfer matrix method [40] in JAX and draws material parameters from a public refractive index database [41]. This enables rapid, large-scale optical simulations as well as efficient gradient-based optimization.

We evaluated suitable low-cost dielectric materials for multilayer structural colors, determined optimal layer thicknesses, and analyzed various stacking configurations [42]. Simulations were conducted over the visible spectrum (350–700 nm) under normal incidence, utilizing the CIE 1931 standard illuminant D65 to represent average daylight. These simulation conditions are maintained throughout this study unless otherwise specified.

2.2 Multistep Inverse Design

We have further developed a multistep inverse design approach to find the optimal multilayer structure for a desired target color [38]. The process begins by using forward simulations to generate a data set of 3125 color-structure data points through a grid search. Each dielectric thickness is swept from 25 nm to 250 nm, producing all combinations of layer thicknesses. Fig. 1a shows an example of such a dataset for an all-dielectric multilayer structure ($TiO_2/SiO_2/TiO_2$) on an Fe substrate coated with a 4 nm thin layer of Fe_3O_4. A decision-tree model is then trained on this dataset, providing an initial structural design whose hue matches the target color. This initial design serves as the starting point for a gradient-based search algorithm, which refines the multilayer composition to achieve a better color match. As shown in Fig. 1b for a primary blue target (blue circle) in the sRGB space, the decision-tree prediction (black circle) is noticeably improved after gradient-based refinement (square blue dot). This multistep approach reduces the likelihood of becoming trapped in local minima, leading to more reliable convergence toward the target color. Finally, by selecting target colors outside the achievable region, this inverse-design framework can also be used to determine the color-gamut limits of any given multilayer architecture.

3 Results and Discussions

3.1 Multilayer Structures with a Single Fabry-Pérot Cavity

The absorption peak of FP cavities can be tuned by varying the thickness of the lossless insulator between the metal layers [37, 31]. We examine the reflective spectra of a single Fabry-Pérot (SFP) cavity ($Cu/TiO_2/FeSub$) as the thickness of TiO_2 is varied (Fig. 2a). These results demonstrate that an SFP cavity is incapable of generating high-purity reflective colors, as it reflects wide-band spectra and only provides narrow-band absorption.

To enhance spectral purity, a TiO_2 anti-reflection layer was introduced atop the SFP cavities to suppress unwanted reflections (Fig. 2b). We investigated three single-cavity multilayer structures, each using TiO_2 as the dielectric spacer, as its high refractive index helps maintain angle-independent coloration. For the metal layers, we compared Ni (Ni-SFP, Fig. 2b(i)), Ti (Ti-SFP, Fig. 2b(ii)), and metal-like ceramic TiN (TiN-SFP, Fig. 2b(iii)).

Using our inverse design framework and setting target colors beyond each structure's achievable range, we determined the maximum color gamut boundaries for all three configurations. As shown in Fig. 2c, the resulting gamuts span most of the sRGB blue region, with pure sRGB blue being achievable, especially for Ni- and Ti-based designs (Fig. 2d(i)). However, none of the structures reach the sRGB green or red primaries. As a result, the closest achievable green and red points remain significantly distant from the sRGB vertices (Figs. 2d(ii) and 2d(iii)).

The reflection spectra for the optimized blue configuration (illustrated in Fig. 2e(i)) indicate that Ni-SFP offers the best performance balance, producing a high spectral purity with approximately 70% peak reflection efficiency. In contrast, Ti-SFP achieves the highest peak efficiency ($\approx 80\%$) at the cost of slightly reduced purity, while TiN-SFP exhibits good purity but suffers from lower peak efficiency ($\approx 50\%$). Consequently, Ni-SFP is identified as the most suitable structure for generating pure blue. For the standard green color (Fig. 2e(ii)), all structures demonstrate high peak reflection efficiencies ($> 70\%$). However, their spectral purity is compromised by parasitic reflection, particularly in the blue region. The red spectra (Fig. 2e(iii)) reveal even more pronounced limitations: all structures exhibit low peak efficiencies ($< 60\%$) and retain significant broadband interference in both the blue and green portions of the spectrum, preventing formation of a pure red.

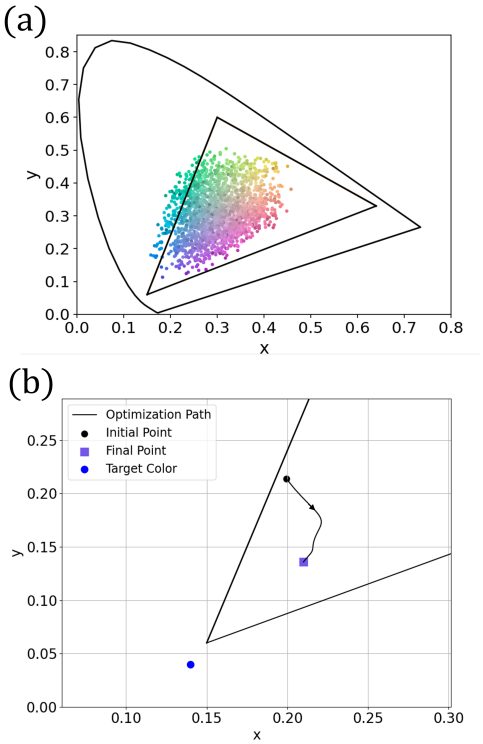

Figure 1. Color gamut optimization framework. (a) Forward simulation results of an all-dielectric multilayer structure ($TiO_2/SiO_2/TiO_2$) on an Fe substrate with various combinations of layer thickness in CIE 1931 color space; (b) Illustration of the inverse-design process in CIE 1931 space: the target color (blue dot), the initial prediction from the decision-tree model (black circle), and the final optimized color after gradient-based refinement (blue square).

In summary, multilayer structures incorporating an SFP cavity and an anti-reflection coating successfully produce pure blue, but fail to yield compliant pure green and red hues. Among the configurations tested, the Ni-based structure (Ni-SFP) exhibits optimal performance for blue generation, providing the best balance of color purity and peak reflection efficiency.

3.2 Multilayer Structures with Dual Fabry-Pérot Cavities

Building on our preliminary analysis of SFP structures and recent findings in the literature [36, 37, 31], we introduce a second FP cavity to create a dual-cavity architecture (DFP). The goal of this design is to suppress more parasitic spectral features responsible for degrading the color purity of green (Fig. 2e(ii)) and red (Fig. 2e(iii)), observed in SFPs. Because the Ni-based cavity (Ni-SFP) produces the highest-purity blue among the single-layer variants, we retain this configuration as the foundation for all dual-cavity designs.

A key challenge in designing the second cavity is selecting a metal that can effectively absorb residual blue light while still transmitting the longer-wavelength green and red reflections produced by the bottom cavity. The most straightforward choice of metal for the upper FP cavity is Ni (designated Ni-Ni-DFP), as illustrated in Fig. 3a(i). However, when optimized for pure blue, the thickness of the upper Ni layer vanishes to zero, reverting the design to the single-cavity configuration of Ni-SFP (Fig. 2a(i)); therefore, the resulting blue color (Fig. 3c(i)) and the corresponding reflection spectra (Fig. 3d(i)) are the same as those of Ni-SFP. While the Ni-Ni-DFP architecture achieves an sRGB-compliant pure green (Fig. 3c(ii)), it suffers from low reflection efficiency ($\approx 50\%$, see Fig. 3d(ii)). Furthermore, it fails to produce an sRGB-compliant red (Fig. 3c(iii)). As indicated by the spectra in Fig. 3c(iii), significant residual reflectance in the blue and green bands degrades the purity of the red color, and the brightness of the red color is also very low due to the low peak reflection efficiency.

Achieving a pure red reflection in dual-cavity structures requires the upper FP cavity to function as a selective spectral filter: its metal layer must transmit red light reflected from the bottom cavity while effectively absorbing blue and green wavelengths. We evaluated the absorption characteristics of candidate metals at a thickness of 50 nm (Fig. 3b(i)), finding that Au and Cu were the only materials exhibiting the requisite spectral behavior (high absorption in short-wavelength and high transparency

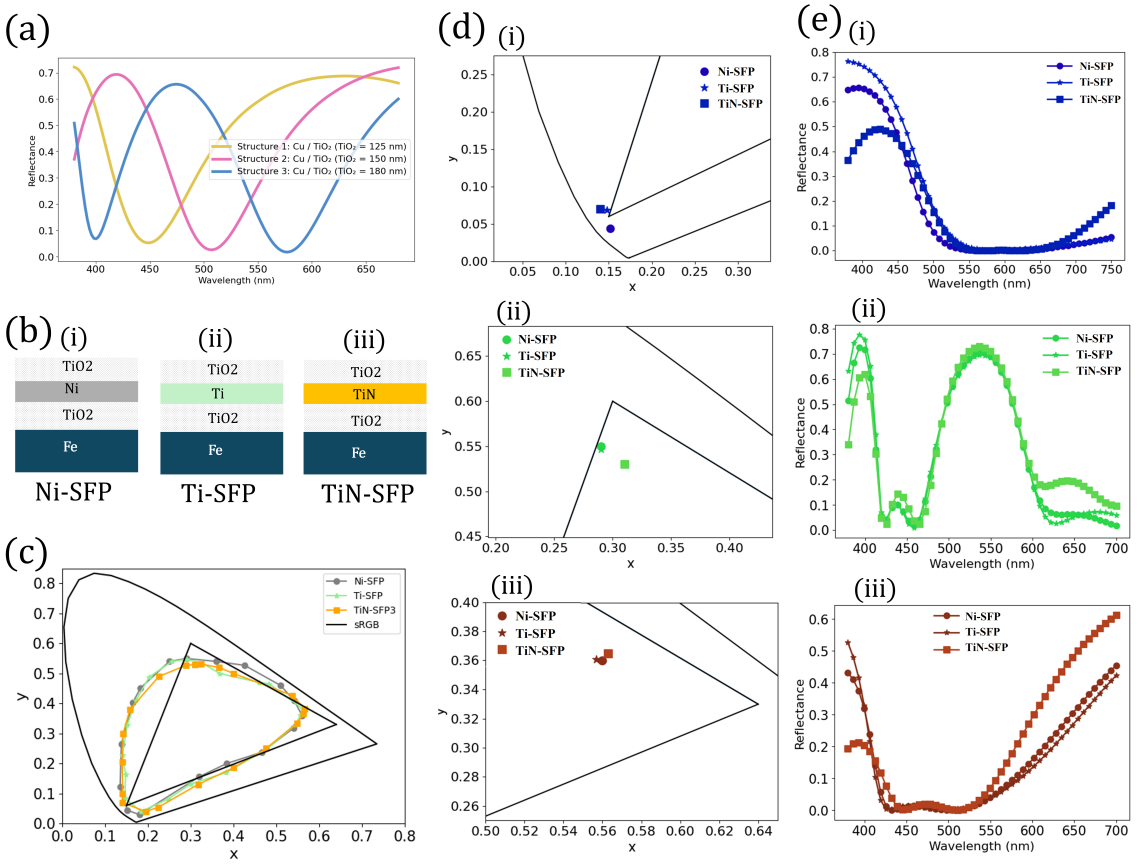

Figure 2. Single Fabry-Pérot (SFP) results. (a) Reflective spectral lines of an SFP cavity with respect to the thickness of the lossless insulator layer; (b) Multilayer structures with an SFP cavity made of different metals, (i) Ni, (ii) Ti, and (iii) TiN on a Fe substrate; (c) Gamut comparison of the three structures proposed in (b); (d) The detailed locations of best achieved blue (i), green (ii), and red (iii) in CIE 1931 space for the three structures proposed in (b); (e) The corresponding spectral lines of structures that achieved best blue (i), green (ii), and red (iii).

in long-wavelength). We selected Cu for the upper cavity (designated Cu-Ni-DFP, Fig. 3a(ii)) as a cost-effective alternative to the noble metal Au. Similar to the Ni-Ni-DFP case, the optimization for pure blue causes the thickness of the upper Cu layer to vanish, reverting the design to the single-cavity Ni-SFP configuration (Fig. 3c(i)). While the Cu-Ni-DFP architecture yields a green hue that exceeds the sRGB saturation (Fig. 3c(ii)), it retains a relatively low peak reflection efficiency ($\approx$ 50%, Fig. 3d(ii)). Crucially, Cu-Ni-DFP successfully produces an sRGB-compliant red (Fig. 3c(iii)) with a satisfactory peak reflection efficiency approaching 70%, as supported by the spectra in Fig. 3d(iii). Consequently, the Cu-Ni-DFP architecture significantly expands the color gamut compared to Ni-Ni-DFP, particularly in the green and red regions (Fig. 3e(i)). Compared to state-of-the-art Feno Resonant Optical Coating (FROC) structures [28], the Cu-Ni-DFP configuration demonstrates greater coverage in the blue and red regions, incurring only a minimal reduction in the green gamut (Figs. 3e(i) and 3e(ii)). Specifically, the Cu-Ni-DFP structure achieves full coverage of the sRGB space (100%) while exceeding the sRGB volume by over 62%, and the color gamut coverage range reaches 54% of the entire CIE 1931 color space. The thickness of each layer in the structure is provided in the Supplementary material.

The low peak reflection efficiency of the Cu-Ni-DFP structure ($\approx$ 50%, Fig. 3d(ii)) in the green region ($\approx$ 550 nm) is mainly attributed to the high absorption (Fig. 3b(i)) and low reflectivity (Fig. 3b(ii)) of the Fe substrate. To enhance the performance in this band, a substrate with lower absorption and higher reflectivity around 550 nm is desirable. Although Ag offers the lowest absorption and highest reflection at this wavelength (Figs. 3b(i) and 3b(ii)), it is an unsuitable candidate due to its high cost and insufficient absorption in the blue region ($\approx$ 470 nm), which is necessary to produce a pure red color. Consequently, we evaluated Au and Cu as the better candidates because they have a high absorption in the blue band and high reflection in the green and red bands ((Figs. 3b(i) and 3b(ii))). We selected Cu as the new substrate material (designated as Cu-Ni-DFP-CuSub, Fig. 3a(iii)), given that it is more cost-effective than the noble metal Au. This Cu substrate can be implemented as a layer thicker than 100 nm deposited on a base such as Fe,

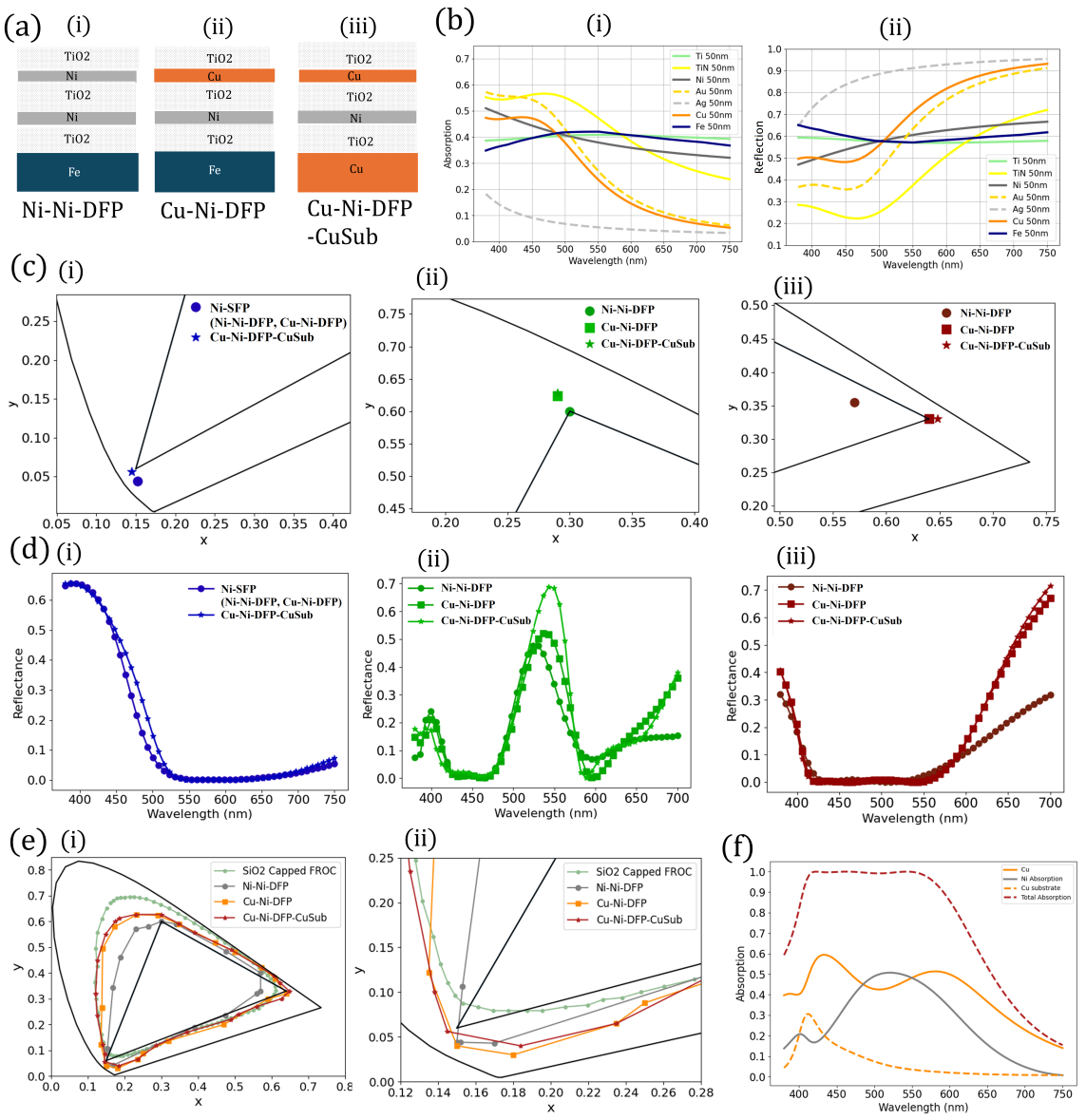

Figure 3. (a) Multilayer structures with dual FP cavities using Ni as absorption metals and Fe as substrate, designated as Ni-Ni-DFP (i), using Ni and Cu as absorption metals and Fe as substrate, designated as Cu-Ni-DFP (ii), using Ni and Cu as absorption metals and Cu as substrate, designated as Cu-Ni-DFP-CuSub (iii); (b) Absorption efficiency (i) and reflection efficiency (ii) of a few metals as a function of wavelength; (c) The coordinates of best achievable pure primary colors from the multilayer structures with dual cavities for blue (i), green (ii), and red (iii) in the CIE 1931 space; (d) The corresponding reflective spectral lines for the best achievable primary colors, blue (i), green (ii), and red (iii); (e) The color gamuts in CIE 1931 space (i) for all structures along with the the SiO_2 capped FROC (extracted from [28]), and a zoom in view (ii) of pure blue region showing results when dual cavities shrunk to single cavity in this band; (f) The total absorption and the absorption of each metal layer in the Cu-Ni-DFP-CuSub structure.

Al, or glass. The resulting Cu-Ni-DFP-CuSub structure significantly improves the green reflection efficiency to 70% (Fig. 3d(ii)). However, it yields only minimal improvement in the overall color gamut compared to Cu-Ni-DFP, with 66% more coverage than the sRGB space (compared to 62% of Cu-Ni-DFP), and 56% coverage of the entire CIE 1931 space (compared to 54% of Cu-Ni-DFP). Therefore, if high-brightness green is not a critical requirement, Cu-Ni-DFP remains the more cost-effective solution. The thickness of each layer in the structure is provided in the Supplementary material.

After checking the absorption for each layer of the Cu-Ni-DFP-CuSub structure that achieved the best pure red result, we noticed that most absorption occurs in the metal layers, as shown in Fig. 3f, confirming the role of FP cavities in suppressing unwanted spectral. In particular, the top Cu layer exhibits the most absorption from blue to green with a peak in the blue region; the Ni layer contributes significantly to absorption in the green region; and the substrate Cu further provides an

absorption peak in the blue region. The other two structures with dual cavities (Ni-Ni-DFP and Cu-Ni-DFP) demonstrate similar results (not shown).

Both configurations demonstrate exceptional performance for pure color generation, achieving 100% coverage of the sRGB space and exceeding the sRGB volume by more than 62% for Cu-Ni-DFP and 66% for Cu-Ni-DFP-CuSub. The color gamut coverage ranges of these two structures reach 54% and 56% of the CIE 1931 color space, respectively. Cu plays a critical role in producing these pure colors by selectively absorbing unwanted blue reflections. Furthermore, the Cu-Ni-DFP-CuSub structure, which yielded the highest color purity, achieves reflection efficiencies of 70% or higher for all primary colors. Although generating highly saturated red (termed Schrödinger's red [26]) remains a challenge in multilayered structures due to higher-order resonances at blue and green wavelengths, our results are highly competitive and promising. Table 1 summarizes the state-of-the-art performance of multilayer-based red structural colors and the corresponding coordinates in CIE 1931 are also plotted in Fig. 4. Our proposed Cu-Ni-DFP-CuSub structure achieves results not only superior to those of state-of-the-art works but with significantly lower cost potential due to the exclusive use of low-cost materials.

Table 1. Comparison of the best red colors achieved for multilayer structures in this work and other state-of-the-art work with available data. * The CIE 1931 coordinates reported here are simulation results from their work, not the experimental results. †For the design reported by Kim et al. [36], the red performance value is estimated from the layer thicknesses provided in their paper, as the publication does not supply sufficient spectral information to quantify the achieved red directly.

Reference	**Structure** top/.../bottom/Substrate	**CIE 1931 Coordinates***
This work	TiO_2/Cu/TiO_2/Ni/TiO_2/Cu	(0.648, 0.329)
Lee *et al* [34]	Si_3N/a-Si/Si_3N/a-Si/Si_3N/a-Si/Si_3N/Glass	(0.64, 0.33)
Kwak *et al* [30]	WO_3/Cr/WO_3/Ag/Glass	(0.64, 0.33)
Yang *et al* [31]	Si_3N_4/Ge/Si_3N_4/Ge/Silica	(0.639, 0.331)
Liu *et al* [32]	SiO/SiO_2/a-Si/SiO_2/Ag/Unknown	(0.63, 0.34)
Ji *et al* [33]	Al_2O_3/a-Si/Cu/a-Si/Al_2O_3/Silica	(0.62, 0.32)
ElKabbash *et al* [28]	SiO_2/Ge/Ag/TiO_2/Ag	(0.61, 0.33)
Kim *et al* [36]	Au/SiO_2/Ti/SiO_2/Cu	(0.60, 0.37)†

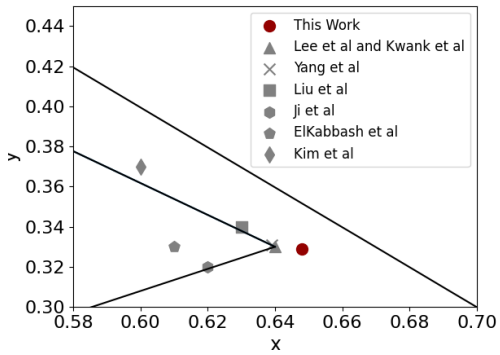

Figure 4. Corresponding CIE 1931 coordinates for all the works listed in Table 1.

3.3 Angle Dependence

We further investigated the color angular dependence of the Cu-Ni-DFP and Cu-Ni-DFP-CuSub structures within the CIE $L^*a^*b^*$ color space. This perceptually uniform space closely reflects human visual sensitivity, where the L^* represents lightness (0=black to 100=white), a^* represents red-green chromaticity (−128 = green to +127=red), and b^* represents blue-yellow chromaticity (−128 =blue to +127=yellow]. To quantify perceptual differences between colors at different viewing angles, we utilized the CIE 2000 ΔE_{00} color difference metric [43, 44]. A ΔE_{00} value of less than 1 is generally imperceptible; values between 1 and 2 are only perceptible under scrutiny; values between 2 and 10 are slightly perceptible; values between 10 and 49 represent noticeable but still similar colors; and values from 49 to 100 correspond to colors that are effectively complementary [45].

Figure 5a presents the sRGB primary color results achieved by the Cu-Ni-DFP-CuSub architecture across a viewing angle range from 0° to 60°. To quantify color variation, we calculated the ΔE_{00} relative to a viewing angle of 0° for red, green, and blue as a function of viewing angle (Fig. 5b).

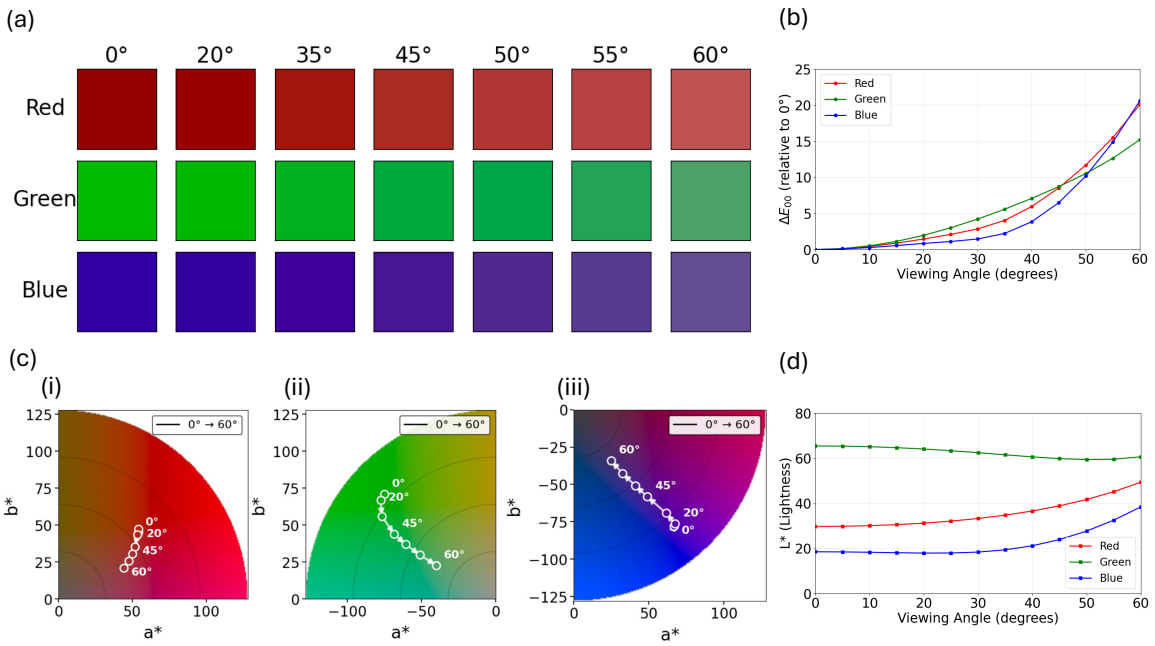

Figure 5. (a) Angular Independency of Cu-Ni-DFP-CuSub structure; (b) ΔE_{00} value of the corresponding colors with respect to viewing angle; (c) Lab space color wheel of 0°, 20°, 35°, 45°, 50°, 55°, 60° for (i) red, (ii) green, (iii) blue; (d) L^*(Lightness) of the corresponding colors with respect to viewing angle

At 20°, the ΔE_{00} values are 1.44 for red, 1.95 for green, and 0.83 for blue. Even at a viewing angle of 45°, the ΔE_{00} values remain moderate, 8.51 for red, 8.69 for green, and 6.47 for blue, suggesting that the color shift is only slightly perceptible. At 60°, the values increase to 20.06, 15.19, and 20.57, respectively. Importantly, even at this extreme angle, the colors maintain their overall hue, exhibiting strong angular stability, where only a modest loss of chromatic sharpness is observed.

To further analyze this stability, we plotted the colors in the 2D projection of $L^*a^*b^*$ color space (Fig. 5c) for (i) red, (ii) green, and (iii) blue. The 2D projection of a^*b^* provides insight into the hue and chroma, which are the derived polar quantities in the a^*b^* plane. From the plots in Fig. 5c, it is evident that all colors exhibit negligible change in hue and chroma up to a 45° viewing angle. This constancy is also confirmed in Fig. 5d, which illustrates the L^* (Lightness) component as a function of the viewing angle. All colors successfully maintain nearly constant individual brightness across the 0° to 45° range.

The primary mechanism behind this high angular independence is the high refractive index of the TiO_2 layers. As established, the reflective color in such thin-film multilayer structures is determined by the optical path difference, which is dictated by the layer thicknesses. For materials possessing a high refractive index, even when the incident angle is large, the optical path difference remains nearly constant relative to normal incidence. Consequently, the structure exhibits minimal perceived color change across a broad range of viewing angles [46]. Since our proposed structure utilizes TiO_2, a high refractive index material, it successfully maintains its perceptible color integrity across a wide span of incident angles. The results for the Cu-Ni-DFP structure (shown in the supplemental text) are nearly the same.

4 Conclusions

We have presented a simulation study on how the incorporation of FP cavities expands the color gamut of multilayered structures. Utilizing both forward simulation and inverse design techniques, we can optimize architectures capable of achieving maximum coloration. Our findings reveal that multilayer structures featuring a single FP cavity are sufficient to generate the sRGB primary blue, but that dual FP cavities are required to achieve the sRGB primary green and red. Detailed analysis confirms that Cu plays a critical role in yielding the pure red color from dual-cavity configurations. Specifically, we identified two low-cost multilayer structures (Cu-Ni-DFP and Cu-Ni-DFP-CuSub) that achieve full coverage of the sRGB space (100%) while exceeding the sRGB volume by over 62% for Cu-Ni-DFP and 66% for Ni-DFP-CuSub. The color gamut coverage ranges of these structures reach 54% and 56% of the CIE 1931 color space, respectively. The performance of these two structures not only surpasses state-of-the-art results in multilayered red coloration but also offers a

significantly lower cost potential due to the exclusive use of readily accessible materials. Furthermore, angle-dependence analysis demonstrates that the structure with the largest color gamut yields a vibrant, angle-independent appearance for incident angles up to ±45°. This study provides valuable guidance for a practical path toward manufacturing high-performance structural colors using low-cost materials, thereby paving the way for broad applications in fields such as display electronics, decoration, and anti-counterfeiting.

Acknowledgments
The authors acknowledged the support from the MDS-Rely Center to conduct this research. The MDS-Rely Center was supported by the National Science Foundation's Industry–University Cooperative Research Center (IUCRC) Program under award EEC-2052662 and EEC-2052776.

Author contributions
A.L. designed the project. G.L. and P.L. supervised the project. J.K developed the forward simulation approach. A.L. developed the inverse design approach, proposed multilayer structures, and performed color analysis and color gamut optimization. A.M performed angle dependence analysis. A.L and A.M. wrote the manuscript with inputs from J.K., G.L., and P.L. All authors discussed the results.

Data availability
JaxLayerLumos: A JAX-based efficient transfer- matrix method framework for optical simulations, https://github.com/JaxLayerLumos/JaxLayerLumos. Refractiveindex.info database of optical constants: https://refractiveindex.info/

References

[1] Soroosh Daqiqeh Rezaei, Zhaogang Dong, John You En Chan, Jonathan Trisno, Ray Jia Hong Ng, Qifeng Ruan, Cheng-Wei Qiu, N. Asger Mortensen, and Joel K.W. Yang. Nanophotonic structural colors. *ACS Photonics*, 8(1):18–33, Jan 2021.

[2] Danyan Wang, Zeyang Liu, Haozhu Wang, Moxin Li, L. Jay Guo, and Cheng Zhang. Structural color generation: from layered thin films to optical metasurfaces. *Nanophotonics*, 12(6):1019–1081, 2023.

[3] Rachel C Thayer and Nipam H Patel. A meta-analysis of butterfly structural colors: their color range, distribution and biological production. *Journal of Experimental Biology*, 226(21), 2023.

[4] Zhiyi Xuan, Junyu Li, Qingquan Liu, Fei Yi, Shaowei Wang, and Wei Lu. Artificial structural colors and applications. *The Innovation*, 2(1), 2021.

[5] Yingjie Li, Jingtian Hu, Yixuan Zeng, Qinghai Song, Cheng-Wei Qiu, and Shumin Xiao. Recent progress on structural coloration. *Photonics Insights*, 3(2):R03, 2024.

[6] Won-Jae Joo, Jisoo Kyoung, Majid Esfandyarpour, Sung-Hoon Lee, Hyun Koo, Sunjin Song, Young-Nam Kwon, Seok Ho Song, Jun Cheol Bae, Ara Jo, Myong-Jong Kwon, Sung Hyun Han, Sung-Han Kim, Sungwoo Hwang, and Mark L. Brongersma. Metasurface-driven oled displays beyond 10,000 pixels per inch. *Science*, 370(6515):459–463, 2020.

[7] Soroosh Daqiqeh Rezaei, Jinfa Ho, Tao Wang, Seeram Ramakrishna, and Joel K. W. Yang. Direct color printing with an electron beam. *Nano Letters*, 20(6):4422–4429, Jun 2020.

[8] Jiao Geng, Liye Xu, Wei Yan, Liping Shi, and Min Qiu. High-speed laser writing of structural colors for full-color inkless printing. *Nature Communications*, 14(1):565, Feb 2023.

[9] Gang Li, Meiying Leng, Shancheng Wang, Yujie Ke, Wei Luo, Huiru Ma, Jianguo Guan, and Yi Long. Printable structural colors and their emerging applications. *Materials Today*, 69:133–159, 2023.

[10] Yasi Wang, Mengjie Zheng, Qifeng Ruan, Yanming Zhou, Yiqin Chen, Peng Dai, Zhengmei Yang, Zihao Lin, Yuxiang Long, Ying Li, Na Liu, Cheng-Wei Qiu, Joel K. W. Yang, and Huigao Duan. Stepwise-nanocavity-assisted transmissive color filter array microprints. *Research*, 2018, 2018.

[11] Chengang Ji, Zhong Zhang, Taizo Masuda, Yuki Kudo, and L. Jay Guo. Vivid-colored silicon solar panels with high efficiency and non-iridescent appearance. *Nanoscale Horizons*, 4:874–880, 2019.

[12] Fengxiang Chen, Ya Huang, Run Li, Shiliang Zhang, Baoshun Wang, Wenshuo Zhang, Xueke Wu, Qinyuan Jiang, Fei Wang, and Rufan Zhang. Bio-inspired structural colors and their applications. *Chem. Commun.*, 57:13448–13464, 2021.

[13] Wenhong Yang, Shumin Xiao, Qinghai Song, Yilin Liu, Yunkai Wu, Shuai Wang, Jie Yu, Jiecai Han, and Din-Ping Tsai. All-dielectric metasurface for high-performance structural color. *Nature communications*, 11(1):1864, 2020.

[14] Zhongyang Li, Serkan Butun, and Koray Aydin. Large-area, lithography-free super absorbers and color filters at visible frequencies using ultrathin metallic films. *ACS Photonics*, 2(2):183–188, Feb 2015.

[15] Jiancun Zhao, Meng Qiu, Xiaochang Yu, Xiaoming Yang, Wei Jin, Dangyuan Lei, and Yiting Yu. Defining deep-subwavelength-resolution, wide-color-gamut, and large-viewing-angle flexible subtractive colors with an ultrathin asymmetric fabry–pérot lossy cavity. *Advanced Optical Materials*, 7(23):1900646, 2019.

[16] Zihao Lin, Shi Zhang, Mengjie Zheng, Yuxiang Long, Zhengmei Yang, Yanming Zhou, and Huigao Duan. Silicon carbide film-based fabry-pérot cavity resonance-enhanced absorption and its application for color filters. *Optical Materials*, 96:109370, 2019.

[17] M. A. Rahman, Yun Hee Kim, So-Hye Cho, Seung Yong Lee, and Ji Young Byun. Realization of structural colors via capped cu-based f–p cavity structure. *Opt. Express*, 29(18):29466–29480, Aug 2021.

[18] Md Abdur Rahman, Dong Kyu Kim, Jong-Kwon Lee, and Ji Young Byun. To realize a variety of structural color adjustments via lossy-dielectric-based fabry–pérot cavity structure. *Nanophotonics*, 11(21):4855–4868, 2022.

[19] Stefano Rossi and Magnus P Jonsson. Highly reflective optical nanocavities for structural coloration by combining broadband absorber and fabry–pérot effects. *Journal of Optics*, 23(1):015001, dec 2020.

[20] Zhengmei Yang, Yanming Zhou, Yiqin Chen, Yasi Wang, Peng Dai, Zhaogang Zhang, and Huigao Duan. Reflective color filters and monolithic color printing based on asymmetric fabry–pérot cavities using nickel as a broadband absorber. *Advanced Optical Materials*, 4(8):1196–1202, 2016.

[21] Harim Oh, Jaeyong Kim, Minseok Seo, Jong-Joo Rha, and Myeongkyu Lee. Structural coloration of stainless steel with planar thin-film surface cavity structure. *Optical Materials*, 100:109547, 2020.

[22] Jaeyong Kim, Harim Oh, Minseok Seo, and Myeongkyu Lee. Generation of reflection colors from metal–insulator–metal cavity structure enabled by thickness-dependent refractive indices of metal thin film. *ACS Photonics*, 6(9):2342–2349, Sep 2019.

[23] Mohamed ElKabbash, Theodore Letsou, Sohail A. Jalil, Nathaniel Hoffman, Jihua Zhang, James Rutledge, Andrew R. Lininger, Chun-Hao Fann, Michael Hinczewski, Giuseppe Strangi, and Chunlei Guo. Fano-resonant ultrathin film optical coatings. *Nature Nanotechnology*, 16(4):440–446, Apr 2021.

[24] Junho Lee, Jaeyong Kim, and Myeongkyu Lee. High-purity reflective color filters based on thin film cavities embedded with an ultrathin ge2sb2te5 absorption layer. *Nanoscale Adv.*, 2:4930–4937, 2020.

[25] Yangbo Lian, Yongzhi Zhang, Furong Liu, Qingyuan Chen, Lulu Zhang, and Boshuo Yin. Structural color of multi-order fabry–perot resonator based on sc0.2sb2te3 enhanced saturated reflection color. *Photonics*, 10(1), 2023.

[26] Zhaogang Dong, Lei Jin, Soroosh Daqiqeh Rezaei, Hao Wang, Yang Chen, Febiana Tjiptoharsono, Jinfa Ho, Sergey Gorelik, Ray Jia Hong Ng, Qifeng Ruan, Cheng-Wei Qiu, and Joel K. W. Yang. Schrödinger's red pixel by quasi-bound-states-in-the-continuum. *Science Advances*, 8(8):eabm4512, 2022.

[27] Kyu-Tae Lee, Daeshik Kang, Hui Joon Park, Dong Hyuk Park, and Seungyong Han. Design of polarization-independent and wide-angle broadband absorbers for highly efficient reflective structural color filters. *Materials*, 12(7):1050, 2019.

[28] Mohamed ElKabbash, Nathaniel Hoffman, Andrew R. Lininger, Sohail A. Jalil, Theodore Letsou, Michael Hinczewski, Giuseppe Strangi, and Chunlei Guo. Fano resonant optical coatings platform for full gamut and high purity structural colors. *Nature Communications*, 14(1):3960, Jul 2023.

[29] Sofia Magkiriadou, Meng Xiao, Miguel A Bandres, Zongfu Yu, Paul J Steinhardt, Shuang Yang, Weining Man, Marian Florescu, Shanhui Fan, Kathleen J Stebe, Eric R Dufresne, et al. Absence of red structural color in photonic glasses, bird feathers, and certain beetles. *Physical Review E*, 90(6):062302, 2014.

[30] Hojae Kwak, Incheol Jung, Dohyun Kim, Seongcheol Ju, Soyoung Choi, Cheolhun Kang, Hyeonwoo Kim, Hyoung Won Baac, Jong G. Ok, and Kyu-Tae Lee. Resonant-mode engineering for additive reflective structural colors with high brightness and high color purity. *Scientific Reports*, 14(1):13694, Jun 2024.

[31] Zhengmei Yang, Wenfeng Li, and Huigao Duan. High-purity and wide-angle reflective structural colors based on an all-dielectric fabry–pérot cavity structure. *Opt. Lett.*, 49(3):594–597, Feb 2024.

[32] Jintong Liu, Kun Feng, Yusi Wang, Qingyuan Li, Nan Chen, and Yikun Bu. High-color-purity, high-brightness and angle-insensitive red structural color. *Chin. Opt. Lett.*, 20(2):021601, Feb 2022.

[33] Chengang Ji, Kyu-Tae Lee, and L. Jay Guo. High-color-purity, angle-invariant, and bidirectional structural colors based on higher-order resonances. *Opt. Lett.*, 44(1):86–89, Jan 2019.

[34] Kyu-Tae Lee, Chengang Ji, Debasish Banerjee, and L. Jay Guo. Angular- and polarization-independent structural colors based on 1d photonic crystals. *Laser & Photonics Reviews*, 9(3):354–362, 2015.

[35] Kun Feng, Qingyuan Li, Jintong Liu, Yusi Wang, Nan Chen, Yankai Li, and Yikun Bu. All-dielectric thin films based on single silicon materials for angle-insensitive structural colors. *Opt. Lett.*, 46(20):5161–5164, Oct 2021.

[36] Do Hyeon Kim, Young Jin Yoo, Joo Hwan Ko, Yeong Jae Kim, and Young Min Song. Standard red green blue (srgb) color representation with a tailored dual-resonance mode in metal/dielectric stacks. *Opt. Mater. Express*, 9(8):3342–3351, Aug 2019.

[37] Amir Ghobadi, Hodjat Hajian, Mahmut Can Soydan, Bayram Butun, and Ekmel Ozbay. Lithography-free planar band-pass reflective color filter using a series connection of cavities. *Scientific Reports*, 9(1):290, Jan 2019.

[38] Anya Li, Jungtaek Kim, Mingxuan Li, Ying Sun, and Paul Leu. Multi-step inverse design optimization for structural colors using dielectric materials. In *2025 IEEE 25th International Conference on Nanotechnology (NANO)*, pages 599–604, 2025.

[39] Mingxuan Li, Jungtaek Kim, and Paul W. Leu. JaxLayerLumos: A JAX-based Differentiable Optical and Radio Frequency Simulator for Multilayer Structures. *Journal of Open Source Software*, 10(114):8572, October 2025.

[40] Leif AA Pettersson, Lucimara S Roman, and Olle Inganäs. Modeling photocurrent action spectra of photovoltaic devices based on organic thin films. *Journal of Applied Physics*, 86(1):487–496, 1999.

[41] Mikhail N. Polyanskiy. Refractiveindex.info database of optical constants. *Scientific Data*, 11(1):94, Jan 2024.

[42] Anya Li, Jungtaek Kim, Mingxuan Li, and Paul W. Leu. Designing multilayered structural colors using low-cost dielectric materials. In *2025 IEEE International Conference on Nano/Micro Engineered and Molecular Systems (NEMS)*, 2025.

[43] M. R. Luo, G. Cui, and B. Rigg. The development of the CIE 2000 colour-difference formula: CIEDE2000. *Color Research & Application*, 26(5):340–350, October 2001.

[44] Gaurav Sharma, Wencheng Wu, and Edul N. Dalal. The CIEDE2000 color-difference formula: Implementation notes, supplementary test data, and mathematical observations. *Color Research & Application*, 30(1):21–30, February 2005.

[45] Zhou Mao, Haiying Qiu, Chingjen Shih, and Zhichong Kang. P-13.12: The Delta E Color Dissimilarity Analysis of LCD Panels. *SID Symposium Digest of Technical Papers*, 55(S1):1404–1414, April 2024.

[46] Zhenzhen Duan, Weijie Chen, Zexiang He, Jian Yang, Guangshi Cai, Haotong Wang, Ning Wang, Zexiong Hu, Dan Wang, Nan Chen, and Yikun Bu. Reflective angle-insensitive structural colors with a wide color gamut employing a Ni/ Ge_2 Sb_2 Te_5 bilayer broadband absorber. *Optics Express*, 32(18):31866, August 2024.